PHOTONICS Research

Three-dimensional nanoscale vortex line visualization and chiral nanostructure fabrication of tightly focused multi-vortex beams via direct laser writing

Mengdi Luo,[1,†] Jisen Wen,[1,†] Pengcheng Ma,[1] Qiuyuan Sun,[1] Xianmeng Xia,[1] Gangyao Zhan,[1] Zhenyao Yang,[1] Liang Xu,[1] Dazhao Zhu,[1,4] Cuifang Kuang,[1,2,3,5] and Xu Liu[2]

[1]Research Center for Intelligent Chips and Devices, Zhejiang Lab, Hangzhou 311100, China
[2]State Key Laboratory of Extreme Photonics and Instrumentation, College of Optical Science and Engineering, Zhejiang University, Hangzhou 310027, China
[3]ZJU-Hangzhou Global Scientific and Technological Innovation Center, Hangzhou 311200, China
[4]e-mail: zhudz@zhejianglab.com
[5]e-mail: cfkuang@zju.edu.cn
[†]These authors contributed equally to this work.

Received 30 June 2023; revised 28 September 2023; accepted 13 October 2023; posted 16 October 2023 (Doc. ID 499405); published 21 December 2023

Optical singularity is pivotal in nature and has attracted wide interest from many disciplines nowadays, including optical communication, quantum optics, and biomedical imaging. Visualizing vortex lines formed by phase singularities and fabricating chiral nanostructures using the evolution of vortex lines are of great significance. In this paper, we introduce a promising method based on two-photon polymerization direct laser writing (2PP-DLW) to record the morphology of vortex lines generated by tightly focused multi-vortex beams (MVBs) at the nanoscale. Due to Gouy phase, the singularities of the MVBs rotate around the optical axis and move towards each other when approaching the focal plane. The propagation dynamics of vortex lines are recorded by 2PP-DLW, which explicitly exhibits the evolution of the phase singularities. Additionally, the MVBs are employed to fabricate stable three-dimensional chiral nanostructures due to the spiral-forward property of the vortex line. Because of the obvious chiral features of the manufactured nanostructures, a strong vortical dichroism is observed when excited by the light carrying orbital angular momentum. A number of applications can be envisioned with these chiral nanostructures, such as optical sensing, chiral separation, and information storage. © 2023 Chinese Laser Press

https://doi.org/10.1364/PRJ.499405

1. INTRODUCTION

Vortex beams have been widely studied due to their phase distributions with singularities, a phenomenon first observed and revealed by Nye and Berry [1]. The vortex beam usually has a phase term denoted by $\exp(im\phi)$, where m is an integer so-called topological charge and ϕ is the azimuthal angle. In 1992, Allen *et al.* proposed that such vortex beams carry orbital angular momentum (OAM) [2], which has furthered the development of vortex beams in various fields, including optical telecommunications [3,4], optical tweezers [5], quantum physics [6,7], and bio-imaging [8–10].

For a conventional vortex beam, the main vortex near the optical axis forms an optical vortex line, which shows stable evolution when it propagates from the near-field to the far-field region in free space. More complex light fields composed of superposition of many plane waves propagating in different directions have been studied for their special vortex evolution trajectories in free space, which is also known as optical vortex knot. The optical knotted nodal lines, as singularities of the wave's phase, determine the topology of the wave field in space. Recent studies have developed various approaches for generating optical vortex knots. In 2010, Dannie *et al.* applied a numerical optimization algorithm to increase the contrast in light intensity to observe several optical vortex knots [11]. Recently, Wang *et al.* designed metasurface holograms to generate optical vortex knots which have a size six orders of magnitude smaller than those produced by a spatial light modulator (SLM) [12].

Besides the generation of optical vortex lines and knots, it is equally important to characterize and visualize them. Previous studies have developed methods to characterize optical vortex lines or knots. The interference method is an efficient approach

to measure the optical vortices but it requires complex configuration for measurement [13]. The saturated-intensity method [14,15] has a rapid speed to locate the optical vortex but loses accuracy compared with the interference method, which locates the positions of phase singularities by interferogram produced by the shaped vortex field and a reference plane wave. Recently, Zhong *et al.* utilized a numerical search algorithm to accurately locate the phase singular points and measure optical vortex links and knots based on digital holography [16].

All mentioned methods are used for the measurement and visualization of the vortex lines or knots nested in optical fields propagating in free space, and little attention has been paid to optical vortex lines or knots in tightly focused light fields. Moreover, it is hard for these methods to find optical vortices at the nanoscale. Therefore, there is a critical need for developing an efficient method to visualize the vortex line, especially in the nanoscale tightly focused light field.

Two-photon polymerization direct laser writing (2PP-DLW) is a promising way to print arbitrary three-dimensional (3D) nanostructures with complex geometry [17–20]. Traditionally, 2PP-DLW fabricates 3D structures in a point-to-point scanning strategy [21,22]. However, this scanning strategy limits fabrication efficiency. In recent years, SLMs have been utilized in 2PP-DLW to directly pattern the shaped light beam to the photoresists, which greatly increases the printing speed [23–25]. In principle, the region where the light intensity of the shaped 3D light field exceeds the power of the threshold of two-photon polymerization is cured to form a 3D structure. Therefore, it has also been employed to record the morphology of various kinds of tightly focused light fields. Up to now, much attention has been paid to fabricating 3D chiral nanostructure based on the optical field intensity distributions including spatially shifted vortex beams [26], double-helix beams [27], superposed Bessel beams [28], and multiramp helico-conical optical beams [29]. Thus, 3D nanostructures fabricated by a single exposure using 2PP-DLW can effectively record the intensity distribution in *xyz* space. Naturally, this raises a question as to whether it is possible to record the vortex line and knot in 3D light field by means of 2PP-DLW.

In this work, we present a novel approach to visualizing the nanoscale tightly focused light fields of MVBs and fabricate 3D chiral nanostructures based on MVBs through single exposure 2PP-DLW. The structure of this paper is organized as follows. We first theoretically and experimentally investigate the tight focusing properties of the MVBs near the focal plane of an oil-immersed high numerical aperture (NA) objective based on Richards–Wolf vectorial diffraction integration. Second, by employing positive photoresist [30] combined with 2PP-DLW, the morphology of vortex lines can be directly recorded, which demonstrates the evolution of optical vortices at the nanoscale. Then we demonstrate efficient fabrications of 3D chiral nanostructures by single exposure on negative photoresist [31]. The diameters and rotation angles of the 3D chiral nanostructures can be flexibly adjusted by varying the parameters of MVBs. Finally, we experimentally measure the optical response of the prepared 3D chiral nanostructures. It is found that the 3D chiral nanostructures exhibit strong vortex dichroism when excited by the continuous laser beam carrying OAM, which may have great importance in optics sensing.

2. TIGHT FOCUSING PROPERTIES OF MVBS

A vortex beam with a helical phase wavefront carries chiral OAM information, but its intensity distribution is a donut-like shape. The vortex beams containing a pair of off-axis vortices at the initial phase plane also have been investigated extensively [32–38]. In this section, we introduce a kind of special vortex beams, named MVBs which possess multiple vortices. After being tightly focused by an oil-immersed high NA objective, the MVBs break the annular intensity distribution and create shaped 3D light fields. The complex field expression of the MVBs at the incident plane of the host Gaussian beam, with beam waist radius w_0, is given by

$$E_i(u,v) = \exp\left(-\frac{u^2+v^2}{w_0^2}\right)\Phi(u,v). \tag{1}$$

(u,v) are the Cartesian coordinates of the incident plane. The MVB is formed by imprinting a phase factor, $\Phi(u,v)$, onto a Gaussian beam, which can be expressed as [39]

$$\Phi(u,v) = \prod_{n'=1}^{|m|}\left[\frac{(u+a\cos\varphi_{n'}) + i(v+a\sin\varphi_{n'})}{\sqrt{(u+a\cos\varphi_{n'})^2+(v+a\sin\varphi_{n'})^2}}\right]^{\mathrm{sign}[m]}, \tag{2}$$

where m is the topological charge and a is the initial off-axis distance of each vortex. sign[∼] represents the sign function and $|\cdot|$ represents absolute value function. $\varphi_n = 2\pi n'/m$ is the azimuthal angle of the n'th singularity.

Figures 1(a1) and 1(a2) show the initial phase profiles of MVBs with different topological charges $m = 2$ and $m = 3$, respectively. The separation and number of vortex cores are adjustable by parameters a and m. Each phase singularity also has a phase ramp from 0 to 2π.

For visualization of the vortex line evolution at the nanoscale and fabrication of nanostructures based on 2PP-DLW, the MVBs need to be tightly focused by a high NA objective. Thus, the analysis of the tight focusing properties is critical. First of all, for simplifying the analysis of the MVBs, the time domain of the femtosecond pulsed beam is ignored. The tightly focusing system is shown in Fig. 1(b).

Given the vectorial nature of the MVBs, in this section, the Richards–Wolf diffraction theory is utilized to describe the tight focusing phenomenon of a high NA objective by calculating the three orthogonal field components E_x, E_y, and E_z. According to the Richards–Wolf vectorial diffraction integration, the tightly focused field can be calculated by

$$\mathbf{E}(\rho,\phi,z) = -\frac{ikf}{2\pi}\int_0^{\theta_{\max}}\int_0^{2\pi}\mathbf{E}(\theta,\varphi,0)T(\theta) \times \mathbf{P}(\theta,\varphi)e^{ik[\rho\sin\theta\cos(\varphi-\phi)+z\cos\theta]}\sin\theta\mathrm{d}\theta\mathrm{d}\varphi, \tag{3}$$

where (ρ,ϕ,z) are the coordinates of the output plane, f is the focal length, and θ is the polar angle of the output pupil ($n\sin\theta_{\max} = \mathrm{NA}$). For the incident plane, $\sqrt{u^2+v^2} = f\sin\theta$ and $\varphi = \arctan(v/u)$. $T(\theta)$ is apodization function

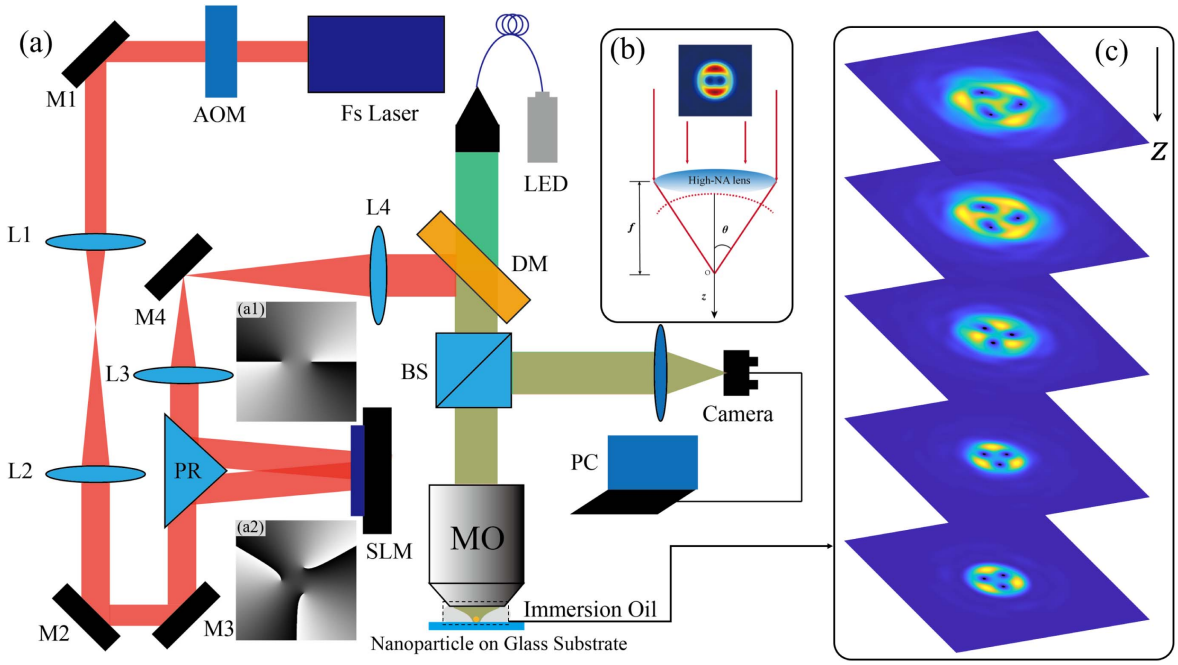

Fig. 1. (a) Scheme of the experimental setup. The MVB is formed by applying phase-only modulation to a Gaussian beam. The initial phase distribution loaded on SLM is demonstrated here with $a = 0.25w_0$, (a1) $m = 2$ and (a2) $m = 3$ as examples. Then, the generated MVB is coupled into a high NA immersion-type objective (MO) and focused onto the sample, consisting of a particle sitting on a glass substrate. The sample is embedded in immersion oil index matched to the substrate. The backward-scattered and reflected light is imaged with a camera. This is also the experimental setup for 2PP-DLW by MVBs. AOM, acousto-optic modulator; M, mirror; HWP, half-wave plate; PBS, polarized beam splitter; L, lens; PR, prism reflector; SLM, spatial light modulator; DM, dichroic mirror; BS, beam splitter. (b) Tight focusing system. (c) Simulated intensity distributions along the propagation direction in the focus region of an objective with NA of 1.45.

(for an aplanatic lens, $T(\theta) = \sqrt{\cos\theta}$) and $\mathbf{P}(\theta, \varphi)$ is the polarization vector, which is set as

$$\mathbf{P}(\theta,\varphi) = \begin{bmatrix} 1 + \cos^2\varphi(\cos\theta - 1) \\ \sin\varphi\cos\varphi(\cos\theta - 1) \\ -\sin\theta\cos\varphi \end{bmatrix} a(\theta,\varphi) + \begin{bmatrix} \sin\varphi\cos\varphi(\cos\theta - 1) \\ 1 + \sin^2\varphi(\cos\theta - 1) \\ -\sin\theta\sin\varphi \end{bmatrix} b(\theta,\varphi). \quad \textbf{(4)}$$

To measure the deformation of the focal spot and reconstruct the focal field distribution, we use a scanning technique in which a gold nanosphere sitting on a glass substrate is utilized as a field probe [40]. The gold nanosphere is scanned through the focal plane by a 3D piezo stage. The objective collects the scattered and reflected light. For each position of the particle relative to the beam, the corresponding image is recorded with a camera. The measured data is utilized to directly showcase the deformation of the focal spot. The experimental setup is shown in Fig. 1(a). Suitable phase masks as shown in Figs. 1(a1) and 1(a2) for creating MVBs are produced using a computer-generated holography (CGH) technique and sent to an SLM. The SLM used in the experiment is a reflection-type phase-modulation SLM (SLM, X15223 – 02 LCOS-SLM, Hamamatsu, Japan) with 1276 × 1024 pixels, 12.5 μm pixel pitch. The active area is 15.9 mm × 12.8 mm. The SLM is illuminated by a femtosecond laser with a center wavelength of 780 nm to produce the desired MVBs. The femtosecond laser source is a Ti:sapphire laser with dispersion precompensation (Chameleon Vision II, Coherent Inc., USA). The pulse duration time and repetition rate of the laser are 140 fs and 80 MHz, respectively.

Combining with Eqs. (1) and (3), the numerical integration allows us to visualize the tight focusing characteristics of the light field generated by MVBs. Figure 2 shows the theoretical and experimental intensity distributions of the MVBs with the indicated topological charge m and initial off-axis distance a at the focal plane ($z = 0$) with NA = 1.45 and $n = 1.518$.

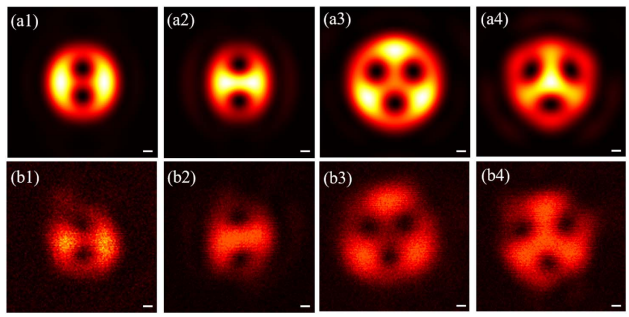

Fig. 2. (a1)–(a4) Theoretical and (b1)–(b4) experimental intensity distributions of the MVBs at the focal plane ($z = 0$) with an oil immersion objective (NA = 1.45, $n = 1.518$) and (a1), (b1) $m = 2$, $a = 0.5$ mm; (a2), (b2) $m = 2$, $a = 0.75$ mm; (a3), (b3) $m = 3$, $a = 0.5$ mm; (a4), (b4) $m = 3$, $a = 0.75$ mm. Scale bar: 100 nm.

Comparing the initial phase distribution in Figs. 1(a1) and 1(a2) with the intensity distribution in Figs. 2(a1) and 2(a3), respectively, an intriguing phenomenon can be found whereby the two vortices of the incident beam locate in the horizontal direction while they locate in the vertical direction in the focal plane. During the tight focusing process by high NA objective, the phase vortices move towards each other when approaching the focal plane and rotate up to $\pi/2$ [33] in the focal plane due to Gouy phase shift [32].

3. VORTEX EVOLUTION RECORDED BY POSITIVE PHOTORESIST

Phase singularities were first recognized as a general phenomenon of wave phase in a seminal paper by Nye and Berry [1]. Optical phase singularities have been a fashionable topic in optical physics for a long time, partly through their relationship with beams carrying orbital angular momentum [2], and a range of techniques have been developed to generate optical fields containing vortices [41]. The evolution of phase vortices where the intensity of the field is equal to zero during tight focusing is an intriguing phenomenon. We experimentally investigate the evolution of the phase vortices along the z direction by patterning the light field in positive photoresist based on 2PP-DLW. The positive photoresist is a type of photoresist in which the portion of the photoresist exposed to light becomes soluble to the photoresist developer [30]. Thus, this kind of photoresist is utilized to record the vortex line evolution and investigate the propagation properties. The 2PP-DLW system in the experiment is schematically shown in Fig. 1(a), which is the same as the gold scanning experimental setup. The simulation and experimental results are shown in Fig. 3.

The numerically determined propagation dynamics of phase vortices are additionally illustrated in Fig. 3(a). Figure 3(b) shows the top view of Fig. 3(a). The phase vortices rotate during tight focusing. It can also be understood by Fig. 3(c) that the positions of the phase vortices denoted by white dots vary with the propagation distance z. To directly demonstrate the evolution of phase singularities, the positive photoresist is employed here to record the 3D vortex line evolution of MVBs in the tight focusing system. Scanning electron microscopy (SEM) is tilted by 30° to show the 3D nanostructures fabricated by a positive photoresist. This nanostructure visualizes the 3D evolution of the vortex line in the xyz space. The inset of Fig. 3(b) is the top view of Fig. 3(d), which is in good agreement with the theoretical results of the vortex line in Fig. 3(b). Despite the existence of aberration in the tightly focusing system, the evolution of phase singularities shown in SEM photos by single exposure on positive photoresist by 2PP-DLW is highly consistent with the numerical results in Fig. 3(b). Thus, it is straightforward to illustrate the 3D vortex line evolution by utilizing positive photoresist-based 2PP-DLW.

Furthermore, we also investigate the evolution of the phase vortices of MVB with $m = 3$, as shown in Fig. 4. Figure 4(a) shows the numerical calculation results of the 3D evolution of phase vortices. The single exposure results on positive photoresist are exhibited in Fig. 4(b). The nanostructure fabricated by positive photoresist is also identical to the theoretical results in Fig. 4.

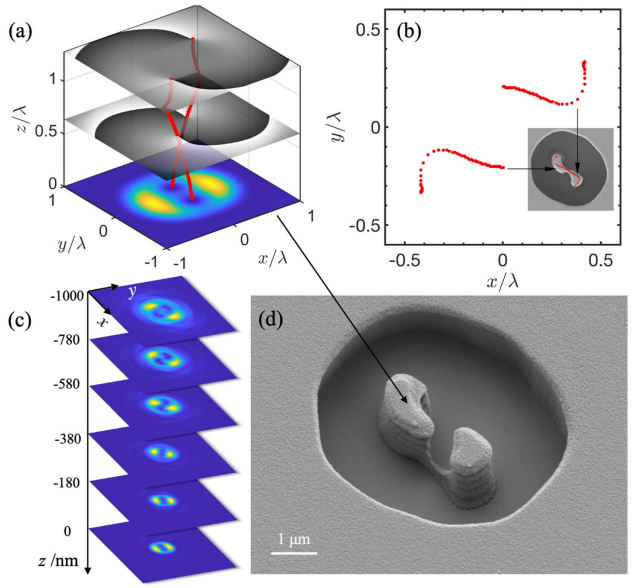

Fig. 3. (a) Visualization of numerically determined 3D evolution of phase vortices. The intensity distribution at the focal plane is also shown. The red dots here represent the vortices. (b) Top view of (a). (c) Numerical results for the evolution of MVBs at different propagation distance z with $m = 2$ and $a = 0.375$ mm in the tight focusing system as shown in Fig. 1(b). Vortices are marked white dots with the indication of corresponding indices. (d) SEM photo of nanostructure of positive photoresist fabricated by single exposure 2PP-DLW recording the evolution of the phase vortices.

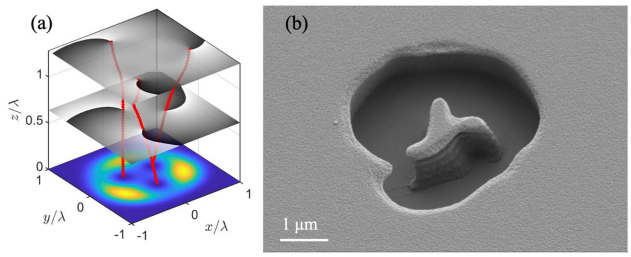

Fig. 4. (a) Numerically calculated results of the evolution of phase vortices with $m = 3$ and $a = 0.375$ mm. The vortices are marked red dots. (b) The 2PP-DLW single-exposure results are observed by SEM.

4. FABRICATION OF CHIRAL 3D NANOSTRUCTURE BASED ON 2PP-DLW

As mentioned in Section 2, the phase vortices rotate during the tight focusing process, forming the shaped 3D light field. Thus, in this section, negative photoresist is utilized to record the intensity evolution based on 2PP-DLW. In the 2PP-DLW experiment, the MVBs are projected into a photoresist sample and complex 3D structures can be fabricated by a single exposure instead of point-to-point scanning. Figures 5(a1), 5(b1), and 5(c1) show the theoretical results of 3D intensity distributions of the MVBs with indicated parameters. The chiral nanostructures and the corresponding arrays fabricated by MVBs are

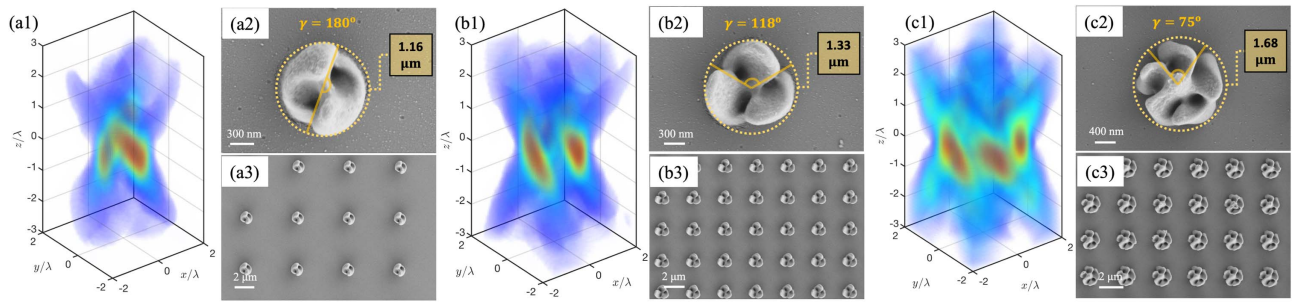

Fig. 5. Propagation evolution and 3D intensity distributions of MVBs with $a = 0.5$ mm and (a1) $m = 2$, (b1) $m = 3$, (c1) $m = 5$. SEM photos of the fabricated 3D chiral nanostructures and the corresponding arrays via tightly focused MVBs with $a = 0.75$ mm and (a2), (a3) $m = 2$; (b2), (b3) $m = 3$; (c2), (c3) $m = 5$.

imaged by SEM as shown in Figs. 5(a2), 5(a3), 5(b2), 5(b3), 5(c2), and 5(c3). The single exposure time (Δt) is 200 ms and the laser power (P) is 10.7 mW. The chiral nanostructures recorded by the photoresist are consistent with the intensity profiles in the xyz plane. The diameter (D) of the nanostructure is relative to the topological charge m. $D = 1.16$ μm with $m = 2$, $D = 1.33$ μm with $m = 3$, and $D = 1.68$ μm with $m = 5$. The diameters of the fabricated structures increase with the increase of m. Furthermore, the subunit of the nanostructure rotates near the focal plane. The rotation angle is defined as γ. The measured rotation angle γ is equal to 180°, 118°, and 75° with $m = 2$, 3, and 5, respectively. The rotation angle is proportional to $1/m$. Therefore, the number of the subunits of the nanostructure and the rotation angle are both dependent on m. The increase of the diameter, number of subunits, and rotation angle match the theoretical results.

Figure 6 shows the effect of the laser power and single exposure time on the diameters of the fabricated structures. The detailed information on the diameter is demonstrated in Fig. 6(b). The diameters increase with the increase of P and Δt, respectively, but are not in a linear relationship. It is demonstrated in Refs. [18,42,43] that D has a relationship as $D \propto \sqrt{\ln P/P_{\text{th}}}$ and $D \propto \sqrt{\ln \Delta t/\Delta t_{\text{th}}}$, where P_{th} is the threshold laser power of 2PP-DLW and Δt_{th} is the threshold single exposure time of 2PP-DLW. It can be explained by the nonlinear process of two-photon polymerization.

The optical response is a significant property for 3D nanostructures. The optical response can be effectively enhanced by 3D nanostructures, which have been applied in various applications including broadband circular polarizers and near-infrared optical rotation devices [44,45]. It is obviously observed in Fig. 5 that the fabricated nanostructures have chiral spatial morphologies, which absolutely cause a strong optical response to OAM. The nanostructures exhibit different optical responses to incident light with opposite OAM. Here, the vortex dichroism is adopted to show such optical response, which is defined as [24]

$$\text{VD} = 2 \times \frac{I_{+l} - I_{-l}}{I_{+l} + I_{-l}} \times 100\%, \tag{5}$$

where I_{+l} and I_{-l} are the reflection intensity of chiral nanostructures under the topological charge of $+l$ and $-l$. In the detection process, the vortex beams with a constant wavelength

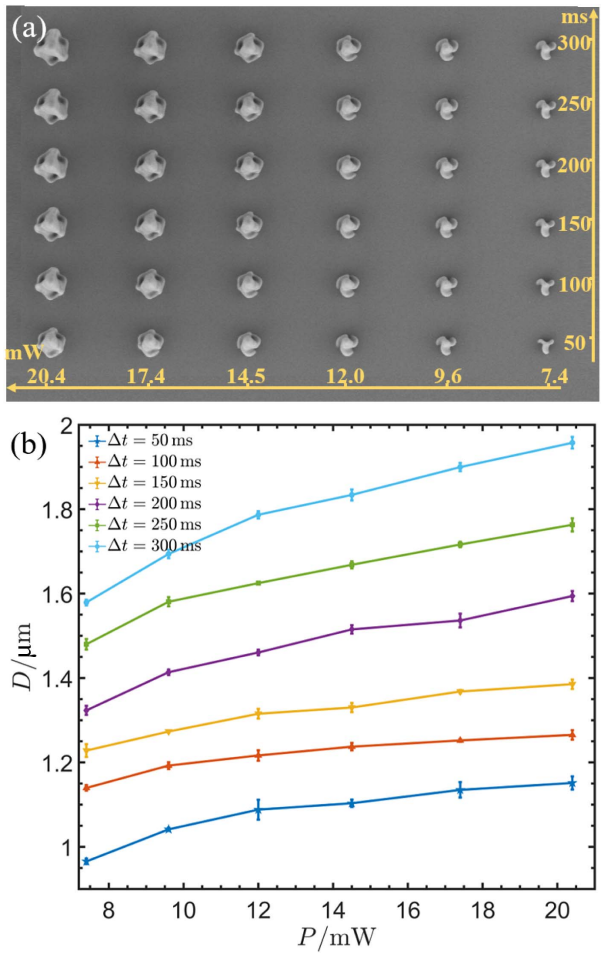

Fig. 6. (a) SEM photos of the fabricated 3D chiral nanostructures with different laser power and single exposure time. (b) Dependence of the diameters of the fabricated nanostructures on the laser power and exposure time.

of 532 nm and a defined topological charge l interact with the chiral nanostructure, causing the change of the discrete OAM spectrum and the generation of VD.

The measurement process of VD is shown in Fig. 7(a). The phase-only SLM is utilized here to modulate the incident

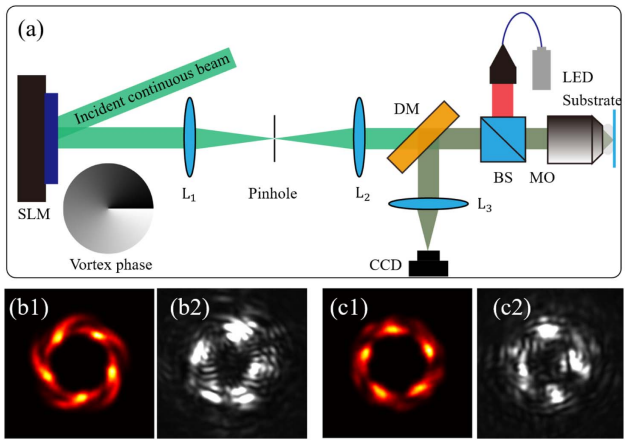

Fig. 7. Principle of measuring vortex dichroism spectra. (a) Experimental setup for measuring VD. The phase-only SLM is used to imprint the vortex phase onto a Gaussian incident continuous beam. Then the vortex beam is tightly focused on the chiral nanostructure through the objective, and the reflected light is collected by CCD. The simulation and experimental results of intensity distributions passing through the nanostructures with (b1), (b2) $l = 10$ and (c1), (c2) $l = -10$ are demonstrated, respectively.

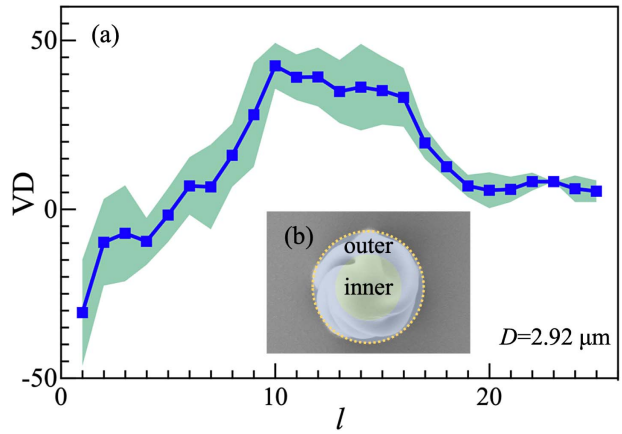

Fig. 8. (a) Optical vortical dichroism measurements of the chiral nanostructure versus topological charge $|l|$. The insert is the SEM photo of the measured nanostructure with $D = 2.92$ μm. (b) SEM photo of the nanostructure with different chiral properties in the inner area and outer area.

continuous beam into a vortex beam. The vortex beam is tightly focused by the objective onto to the nanostructure and then the reflected light is collected by CCD. The measured VD spectrum of the nanostructure [SEM photo is exhibited in Fig. 8(b)] with $D = 2.92$ μm and the glass substrate is shown in Fig. 8(a). The chiral nanostructure is fabricated by the MVB with $m = 5$, $a = 0.75$ mm, the laser power is 40 mW, and the single exposure time is 200 ms. The finite difference time domain (FDTD) method is employed to simulate the light intensity distributions passing through the nanostructure. The results are shown in Figs. 7(b1) and 7(c1). The excitation incident vortex beam is with $l = \pm 10$. Figures 7(b2) and 7(c2) exhibit the experimental results, which are highly consistent with the simulation. Obviously, the intensity profile with $l = 10$ is stronger than that with $l = -10$. Thus, the optical vortex dichroism varies with topological charge.

By scanning the topological charges of the incident vortex beam from −25 to +25, the VD versus l on the nanostructure is demonstrated in Fig. 8(a). The error of the signal is caused by factors such as uneven energy distributions of the excitation vortex beam, imperfect structural space symmetry, system aberration, system vibration, and shift. Nevertheless, the experimental results still well demonstrate the chiral nanostructure responses to the spiral phase. It can be seen that the VD peak occurs at the topological charge of 10. The magnitude of VD can approach approximately 42%. When $l < 7$, the magnitude of VD is negative, which means the total intensity of the vortex excitation beam with a positive topological charge is weaker than that with a negative one. This strange phenomenon results from the different chiral properties with various parts of the nanostructure. The chiral nanostructure can be divided into two parts, named inner and outer area, as shown in Fig. 8(b). The vortex beam spot generally increases with the increase of topological charge. Thus, the excitation vortex beams mainly pass through the inner area of the nanostructure. With the increase of l, the excitation vortex beam and the nanostructure interact in the outer area. Then, the VD reaches the peak when the incident vortex beam has a topological charge l near 10, which is affected by experimental errors. Finally, when the vortex beam focal spot is larger than the nanostructure, i.e., there is no interaction between the vortex beam and chiral nanostructure, the VD is therefore almost equal to zero.

After modulation by the fabricated nanostructure, it is necessary to analyze the optical properties of the reflected vortex beam. Thus, we intend to discuss the significant OAM spectrum of the modulated beam. The discrete OAM spectrum is employed here. The complex amplitude of the reflected beam can be expanded into an angular-harmonic series [46]:

$$E_{\mathrm{ref}} = \sum_{p=-\infty}^{\infty} E_p \exp(ip\phi_p). \tag{6}$$

The complex amplitude of each angular harmonic is given by

$$W_p = \frac{\left|\int_{-\infty}^{+\infty}\int_{-\infty}^{+\infty} E_{\mathrm{ref}} \exp(-ip\phi_p)\mathrm{d}x\mathrm{d}y\right|^2}{\sum_{p=-\infty}^{\infty}\left|\int_{-\infty}^{+\infty}\int_{-\infty}^{+\infty} E_{\mathrm{ref}} \exp(-ip\phi_p)\mathrm{d}x\mathrm{d}y\right|^2}, \tag{7}$$

where W_p represents the weight of each angular harmonic and p is an integer. The incident beam is a pure OAM beam with a definite topological charge l and a perfect ring-like intensity profile. After interacting with the chiral nanostructure, the reflected beam retains the topological properties well. The discrete numerically calculated OAM spectrum is shown in Fig. 9. The reflected mode is in the superposition states of multiple eigenstates, but the weight of the incident mode is always higher than 0.8 [see in Figs. 9(a) and 9(b), or Figs. 9(c) and 9(d)]. Furthermore, the OAM spectrum of the reflected beams with opposite incident modes is not symmetrical, caused by the VD phenomenon.

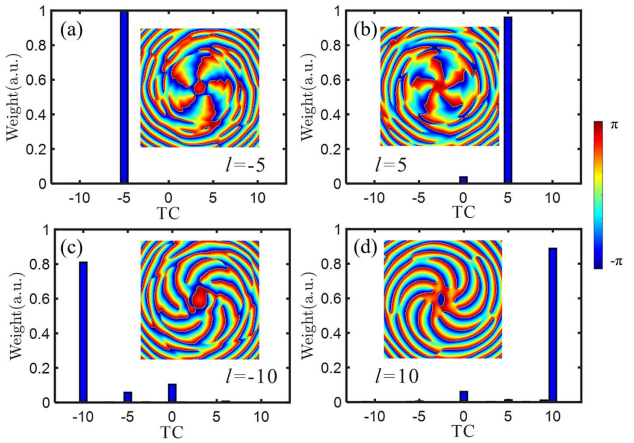

Fig. 9. OAM spectrum analysis of the reflected OAM beams with different incident topological charges: (a) $l = -5$; (b) $l = 5$; (c) $l = -10$; (d) $l = 10$. The insert figures are the respective phase distributions.

5. CONCLUSION

In summary, we both theoretically and experimentally investigate the tightly focused light field of multi-vortex beams with various topological charges and off-axis distances. Due to Gouy phase shift, the vortices in the light field of MVBs move towards each other to the focal plane and rotate during the focusing process. The positive photoresist combined with single exposure based on 2PP-DLW is utilized to visualize the propagation dynamics of phase vortices at the nanoscale. The experimental results are highly consistent with the theoretical simulations. It is a new and efficient method to reveal the vortex line evolution at the nanoscale. According to the intriguing rotation properties of the phase vortices, to form the shaped 3D light fields, we employ the MVBs to efficiently fabricate 3D chiral nanostructures. The nanostructures and their arrays are manufactured by a single exposure on negative photoresist via 2PP-DLW. The dependence of the diameters of the fabricated structures on the laser power and single exposure time, and the rotation angle on the topological charge, are additionally demonstrated. Furthermore, the fabricated 3D chiral nanostructures exhibit strong vortex dichroism when excited by the vortex beams carrying OAM. The optical vortex dichroism is therefore measured. The fabrication strategy proposed in this paper can efficiently obtain 3D chiral nanostructures with a high throughput. This method can also be generalized to exploit more complex optical beams, for example, beams with specific polarization singularities. It may have wide applications in the fields of optical sensing, advanced functional devices, and so on.

Funding. National Key Research and Development Program of China (2021YFF0502700); China Postdoctoral Science Foundation (2022M722905); Zhejiang Provincial Ten Thousand Plan for Young Top Talents (2020R52001); Major Program of Natural Science Foundation of Zhejiang Province (LD21F050002); "Pioneer" and "Leading Goose" Research and Development Program of Zhejiang Province (2023C01051, 2023C01186).

Acknowledgment. The authors acknowledge constructive discussions from Dr. Shangting You and Dr. Xi Liu on result analysis.

Disclosures. The authors declare no conflicts of interest.

Data Availability. The data that support the plots within this paper and other findings of this study are available from the corresponding author upon reasonable request.

REFERENCES

1. J. F. Nye and M. V. Berry, "Dislocations in wave trains," Proc. R. Soc. London Ser. A Math. Phys. Eng. Sci. **336**, 165–190 (1974).
2. L. Allen, M. W. Beijersbergen, and R. J. Spreeuw, *et al.*, "Orbital angular momentum of light and the transformation of Laguerre-Gaussian laser modes," Phys. Rev. A **45**, 8185–8189 (1992).
3. F. Yue, D. Wen, and C. Zhang, *et al.*, "Multichannel polarization-controllable superpositions of orbital angular momentum states," Adv. Mater. **29**, 1603838 (2017).
4. T. Lei, M. Zhang, and Y. Li, *et al.*, "Massive individual orbital angular momentum channels for multiplexing enabled by Dammann gratings," Light Sci. Appl. **4**, e257 (2015).
5. T. Kuga, Y. Torii, and N. Shiokawa, *et al.*, "Novel optical trap of atoms with a doughnut beam," Phys. Rev. Lett. **78**, 4713–4716 (1997).
6. S. Oemrawsingh, A. Aiello, and E. Eliel, *et al.*, "How to observe high-dimensional two-photon entanglement with only two detectors," Phys. Rev. Lett. **92**, 217901 (2004).
7. S. Oemrawsingh, X. Ma, and D. Voigt, *et al.*, "Experimental demonstration of fractional orbital angular momentum entanglement of two photons," Phys. Rev. Lett. **95**, 240501 (2005).
8. E. Rittweger, K. Y. Han, and S. E. Irvine, *et al.*, "STED microscopy reveals crystal colour centres with nanometric resolution," Nat. Photonics **3**, 144–147 (2009).
9. J. Hanne, H. J. Falk, and F. Görlitz, *et al.*, "STED nanoscopy with fluorescent quantum dots," Nat. Commun. **6**, 7127 (2015).
10. G. Vicidomini, P. Bianchini, and A. Diaspro, "STED super-resolved microscopy," Nat. Methods **15**, 173–182 (2018).
11. M. R. Dennis, R. P. King, and B. Jack, *et al.*, "Isolated optical vortex knots," Nat. Phys. **6**, 118–121 (2010).
12. L. Wang, W. Zhang, and H. Yin, *et al.*, "Ultrasmall optical vortex knots generated by spin-selective metasurface holograms," Adv. Opt. Mater. **7**, 1900263 (2019).
13. S. J. Tempone-Wiltshire, S. P. Johnstone, and K. Helmerson, "Optical vortex knots - one photon at a time," Sci. Rep. **6**, 24463 (2016).
14. J. Leach, M. R. Dennis, and J. Courtial, *et al.*, "Laser beams: knotted threads of darkness," Nature **432**, 165 (2004).
15. K. O'Holleran, F. Flossmann, and M. R. Dennis, *et al.*, "Methodology for imaging the 3D structure of singularities in scalar and vector optical fields," J. Opt. A **11**, 094020 (2009).
16. J. Zhong, S. Qi, and S. Liu, *et al.*, "Accurate and rapid measurement of optical vortex links and knots," Opt. Lett. **44**, 3849–3852 (2019).
17. D. Gonzalez-Hernandez, S. Varapnickas, and A. Bertoncini, *et al.*, "Micro-optics 3D printed via multi-photon laser lithography," Adv. Opt. Mater. **11**, 2201701 (2022).
18. A. Balena, M. Bianco, and F. Pisanello, *et al.*, "Recent advances on high-speed and holographic two-photon direct laser writing," Adv. Funct. Mater. **33**, 2211773 (2023).
19. I. Bernardeschi, M. Ilyas, and L. Beccai, "A review on active 3D microstructures via direct laser lithography," Adv. Intell. Syst. **3**, 2100051 (2021).
20. H. Wang, W. Zhang, and D. Ladika, *et al.*, "Two-photon polymerization lithography for optics and photonics: Fundamentals, materials, technologies, and applications," Adv. Funct. Mater. **33**, 2214211 (2023).
21. D. Zhu, L. Xu, and C. Ding, *et al.*, "Direct laser writing breaking diffraction barrier based on two-focus parallel peripheral-photoinhibition lithography," Adv. Photon. **4**, 066002 (2022).

22. T. C. Chong, M. H. Hong, and L. P. Shi, "Laser precision engineering: from microfabrication to nanoprocessing," Laser Photon. Rev. **4**, 123–143 (2010).
23. X. Lu, X. Wang, and S. Wang, *et al.*, "Polarization-directed growth of spiral nanostructures by laser direct writing with vector beams," Nat. Commun. **14**, 1422 (2023).
24. D. Pan, S. Liu, and J. Li, *et al.*, "Rapid fabrication of 3D chiral microstructures by single exposure of interfered femtosecond vortex beams and capillary-force-assisted self-assembly," Adv. Funct. Mater. **32**, 2106917 (2021).
25. Y. Hu, H. Yuan, and S. Liu, *et al.*, "Chiral assemblies of laser-printed micropillars directed by asymmetrical capillary force," Adv. Mater. **32**, e2002356 (2020).
26. H. Lin and M. Gu, "Creation of diffraction-limited non-airy multifocal arrays using a spatially shifted vortex beam," Appl. Phys. Lett. **102**, 084103 (2013).
27. S. J. Zhang, Y. Li, and Z. P. Liu, *et al.*, "Two-photon polymerization of a three dimensional structure using beams with orbital angular momentum," Appl. Phys. Lett. **105**, 061101 (2014).
28. L. Yang, D. Qian, and C. Xin, *et al.*, "Two-photon polymerization of microstructures by a non-diffraction multifoci pattern generated from a superposed Bessel beam," Opt. Lett. **42**, 743–746 (2017).
29. J. Wen, Q. Sun, and M. Luo, *et al.*, "Fabrication of chiral 3D microstructure using tightly focused multiramp helico-conical optical beams," Micromachines **13**, 1771 (2022).
30. H. Z. Cao, M. L. Zheng, and X. Z. Dong, *et al.*, "Two-photon nanolithography of positive photoresist thin film with ultrafast laser direct writing," Appl. Phys. Lett. **102**, 201108 (2013).
31. C. Cao, Y. Qiu, and L. Guan, *et al.*, "Dip-in photoresist for photoinhibited two-photon lithography to realize high-precision direct laser writing on wafer," ACS Appl. Mater. Interfaces **14**, 31332–31342 (2022).
32. G. Indebetouw, "Optical vortices and their propagation," J. Mod. Opt. **40**, 73–87 (1993).
33. Z. Chen, J. Pu, and D. Zhao, "Tight focusing properties of linearly polarized Gaussian beam with a pair of vortices," Phys. Lett. A **375**, 2958–2963 (2011).
34. M. Chen and F. S. Roux, "Accelerating the annihilation of an optical vortex dipole in a Gaussian beam," J. Opt. Soc. Am. A **25**, 1279–1286 (2008).
35. S. G. Reddy, S. Prabhakar, and A. Aadhi, *et al.*, "Propagation of an arbitrary vortex pair through an astigmatic optical system and determination of its topological charge," J. Opt. Soc. Am. A **31**, 1295–1302 (2014).
36. X. Zhao, X. Pang, and J. Zhang, *et al.*, "Transverse focal shift in vortex beams," IEEE Photon. J. **10**, 6500417 (2018).
37. B. K. Singh, M. Bahl, and D. S. Mehta, *et al.*, "Study of internal energy flows in dipole vortex beams by knife edge test," Opt. Commun. **293**, 15–21 (2013).
38. J. Wen, B. Gao, and G. Zhu, *et al.*, "Precise position and angular control of optical trapping and manipulation via a single vortex-pair beam," Opt. Lasers Eng. **148**, 106773 (2022).
39. Z. Mei, Y. Mao, and J. Wang, *et al.*, "Spatial correlated vortex arrays," Opt. Express **31**, 727–736 (2022).
40. M. Neugebauer, P. Banzer, and T. Bauer, *et al.*, "Geometric spin Hall effect of light in tightly focused polarization-tailored light beams," Phys. Rev. A **89**, 013840 (2014).
41. Y. Shen, X. Wang, and Z. Xie, *et al.*, "Optical vortices 30 years on: OAM manipulation from topological charge to multiple singularities," Light Sci. Appl. **8**, 90 (2019).
42. T. Baldacchini, *Three-Dimensional Microfabrication Using Two-Photon Polymerization: Fundamentals, Technology, and Applications* (William Andrew, 2015).
43. S. Kawata, H. B. Sun, and T. Tanaka, *et al.*, "Finer features for functional microdevices," Nature **412**, 697–698 (2001).
44. J. K. Gansel, M. Thiel, and M. S. Rill, *et al.*, "Gold helix photonic metamaterial as broadband circular polarizer," Science **325**, 1513–1515 (2009).
45. M. Hentschel, M. Schaferling, and X. Duan, *et al.*, "Chiral plasmonics," Sci. Adv. **3**, e1602735 (2017).
46. V. V. Kotlyar and A. A. Kovalev, "Optical vortex beams with a symmetric and almost symmetric OAM spectrum," J. Opt. Soc. Am. A **38**, 1276–1283 (2021).